Optics & Laser Technology 180 (2025) 111521

Contents lists available at ScienceDirect

Optics and Laser Technology

journal homepage: www.elsevier.com/locate/optlastec

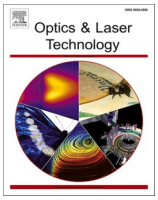

Full length article

Experimental and numerical study of melt flow, temperature behavior and heat transfer mechanisms during the dissimilar laser welding process

Jie Zhang [a,*], Mohammad Hossein Razavi Dehkordi [b,c], Mohammad Javad Kholoud [b], Hamidreza Azimy [b,*], Saeed Daneshmand [d]

[a] School of Mechanical and Electrical Engineering, Hefei Technology College, Hefei 230012, China
[b] Department of Mechanical Engineering, Najafabad Branch, Islamic Azad University, Najafabad, Iran
[c] Aerospace and Energy Conversion Research Center, Najafabad Branch, Islamic Azad University, Najafabad, Iran
[d] Department of Mechanical Engineering, Isfahan (Khorasgan) Branch, Islamic Azad University, Isfahan, Iran

ARTICLE INFO

Keywords:
Dissimilar laser welding
Finite volume method
Temperature distribution
Melt flow
Gaussian heat flux

ABSTRACT

The influence of laser beam deviation on temperature field and melt flow during laser welding of two different metals, brass and 308 stainless steel (S.S 308), was examined numerically and experimentally in this study. The laser beam's absorbed energy was estimated using surface and volumetric Gaussian heat fluxes. While the laser beam's placement on the 308 stainless steel sheet, specifically at a distance of 0.5 mm from the joint, the simulation findings indicated that the temperature differential on the steel's surface was considerably more pronounced than the laser beam was positioned elsewhere. The molten pool's surface tension gradient and buoyancy forces are conducted to form a Marangoni flow. The low melting point of the brass alloy resulted in an enormous molten pool volume than stainless steel under a 0.0 mm beam deviation. Furthermore, the velocity of the melt flow rose by 0.0102 m/s due to an increase in temperature gradient and shear stress yielded by the laser beam's deflection towards the stainless steel sheet. Furthermore, the numerical results coordinated well with the experimental outcomes.

1. Introduction

In order to make a part, many parameters need to be considered. To make a huge and functional part, it is mainly necessary to connect small parts to each other. Therefore, one of the important processes in the preparation of parts before joining is the cutting process [1]. Scientists have proposed various methods in recent years. Numerical simulations, optimization methods, and artificial neural networks (ANNs) can enable new research and industrial applications become more accurate, efficient, and cost-effective [2–4]. Resource optimization and complicated system analysis are possible with numerical simulations [5–7]. One can utilize optimization techniques to determine which solutions are optimal for a given problem. Making predictions and analyzing data with ANNs enables decision-making that is more well-informed [8–10]. Researchers and engineers can obtain insights into the behavior of systems and processes and make well-informed decisions that can result in better outcomes by incorporating numerical simulations, optimization techniques, and artificial neural networks (ANNs) into new studies and industrial applications [11–13]. Also, one of the practical processes is the use of high-power optical photons. The process of using these rays is called the laser process, which is widely used in welding and cutting parts [14]. In this method, a powerful and focused light with high energy density beams on the workpiece, and the cutting or welding process is done. The reason for the popularity of this method among researchers and industries is the high percentage of heat loss in depth to the width of the workpiece. For this reason, this method has gained a special place among researchers in recent years and has become widespread in various industries such as automobile industries, medical industries, pharmaceutical industries, constructions, marine industries, and laboratory sciences [15–17]. Considering that materials with different properties are found in nature, a very suitable and practical structure can be achieved in the laser process by connecting different materials to each other. Thus, considering that these materials are combined in the fusion zone, it is very important to check the properties of the base matrix and the influence of laser parameters on it. Various numerical and experimental methods can be used to analyze the structure and quality of welding. Numerical methods used include simulation [18], artificial neural network [19–22], response surface method [23], and

* Corresponding authors.
E-mail addresses: zhangjie7910@163.com (J. Zhang), hamidrezaazimy@gmail.com (H. Azimy).

https://doi.org/10.1016/j.optlastec.2024.111521
Received 2 April 2024; Received in revised form 25 June 2024; Accepted 24 July 2024
Available online 2 August 2024

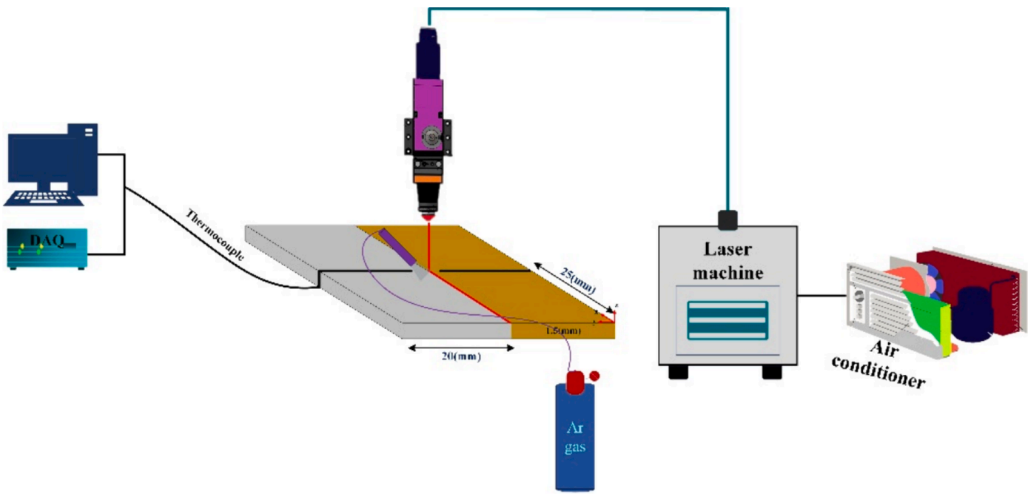

Fig. 1. Laser welding procedure illustration.

optimization [20,24,25]. Also, by using the process optimization method, it is possible to improve the quality and welding structure and reduce production costs.

Sun et al. [26] looked into the impact of laser parameters by numerically simulating the distribution of temperature in the dissimilar laser welding procedure. An artificial neural network (ANN) approach was also used in this process. The simulation findings revealed that raising the pulse width increases the heat transfer quantity and the molten pool's temperature. In addition, lowering the frequency reduces weld penetration depth. Furthermore, the findings of ANN indicated that the parameters of workpiece thermal conductivity coefficient, pulse frequency, and rising process duration substantially influenced laser welding. Oliveira et al. [27] analyzed the quality of laser welding of CoCrFeMnNi to 316 stainless steel. Their results showed that the fusion zone has good strength and mechanical properties due to the presence of coarse grains.

In a numerical analyze, Yan et al. [28] scrutinized the changes in the temperature distribution and residual stress in laser welding. Their outcomes proved that the simulated temperature field agrees with the geometrical morphology of the actual weld metal, and the temperature declines with raised oscillation frequency. Evdokimov et al. [29] analyzed the thermomechanical properties of steel and aluminum mixture in the fusion zone in the simulation of a laser welding process. By presenting models in the laser welding, they proved that the accuracy of thermomechanical simulations can be significantly improved. Jin et al. [30] evaluated the impact of laser welding power input on junction strength, microstructure, and bending properties of Al-steel junctions. Their modeling results revealed that the interfacial temperature changes along the surface area and lowers from the weld's root to the weld's toe. Ding et al. [31] experimentally evaluated the impact of different parameters, for example, welding speed, pulse width, and pulse frequency, on weld dimension and temperature distribution for 308 stainless steel and brass alloys. Their outcomes revealed that according to the value of the thermal conductivity of brass, a molten pool is formed asymmetrically. Welding power and speed were identified as the most critical influencing parameters.

Huang et al. [32] optimized the weld strength using the Taguchi method for dissimilar joining of steel to PMMA. Their results showed that maximum welding strength can be reached using this method. Xin et al. [33] researched the mechanical properties and microstructure of the fusion zone of copper and 316L in the laser welding process. The results confirmed that the use of this approach does not lead to any defects in welding or spherical particles in the molten zone. Xia et al. [34] Analyzed the consequence of different laser beam models on welding quality and developed good numerical models. The results demonstrated that the parameters of peak temperature, temperature gradient, and interaction time are among the parameters affected by the type of laser beam. Ragavendran et al. [35] exanimated the differences between hybrid laser-tungsten inert gas (HLT) and hybrid laser-metal inert gas (HLM) by examining the microhardness of the weld area and its mechanical properties. Their results showed that HLM welding has higher tensile strength, yield strength, and ultimate ductility compared to other methods. Pańcikiewicz et al. [36] examined the inhomogeneous joining quality of two martensitic and austenitic alloys in the laser welding technique. Their findings showed that the hardness in the heat-affected zone (HAZ) of austenitic steel falls while juxtaposed with the base metal and increases when compared to martensitic steel. Assemblies of dissimilar materials by laser welding for electric vehicle battery systems are extensively used to connect several thousand interconnect joints. Laser welding is considered a desirable choice for EV battery manufacturing due to its non-contact nature, high energy density, precise control over the heat input and ease of automation. Developments in dissimilar laser welding of steel-copper, steel-aluminum, aluminum-copper, and steel-nickel, some of the potential joint combinations in battery pack manufacturing [37].

This study provided a comprehensive investigation in welding of two dissimilar materials of austenitic stainless steel 304 and CuZn39Pb3 brass alloy. Because of different chemical and physical properties of both metals, dissimilar laser welding of these alloys has been more challengeable. Extensive evaporation of zinc element in brass alloy clearly induce intensive cavitation and plasma plume during laser welding. Additionally, lower melting point of brass alloy about 500 °C can cause extra melting rate and thereby evaporation of brass alloy in comparison to 304 stainless steel. This phenomenon can alter the stability of laser welding process and appropriate fusion rate of both metals. Therefore, the produced weld characterizations including the fusion zone microstructure, weld bead geometry and the resultant mechanical strength of the dissimilar weld joint has evidently remarkable fluctuation along the weld line. In order to reduce the mentioned drawbacks during welding, the numerical and experimental investigation in welding between two metals was carried out in this analysis to produce the acceptable weld quality with minimum defects which is highly dependent on the criteria used during the laser welding process.

2. Experimental procedure

The laser source for the experiment utilized a pulsed Nd: YAG laser with a highest mean output power of 700 W and an effective wavelength of 1.06 μm. The laser parameters varied from 0.2 to 25 ms in pulse width, 1–250 Hz in frequency, and 0–40 J in energy. The plate's

Table 1
Chemical composition of S.S 308 and brass alloy.

Composition		C%	Cu%	Zn%	Cr%	Mn%	P%	Si%	Ni%	Fe%
Weight	S.S 308	0.03			19.5	2	0.03	0.6	9	Balanced
	Brass		56.7	39.8			0.03		0.08	0.1

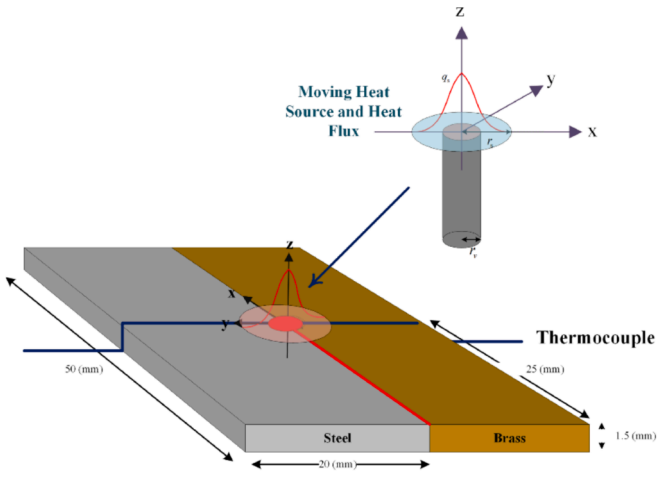

Fig. 2. A diagram of the laser welding process and its thermal energy model.

surface's spot radius was around 0.4 mm. The temperature was detected using K-type thermocouples with tip diameter of 1 mm that measures temperature with an operating temperature range of −40 °C to + 1351 °C and a measurement accuracy of 6 %. On each workpiece a groove with diameter of 1 mm and depth of 0.8 mm was engraved by electro discharge machining (EDM) to located the thermocouple at specific position. The data was collected using a data capture card (Advantech USB 4718). The size of the molten pool was determined employing an Olympus SZ-X16 stereoscopic microscope after metallographic analysis. Fig. 1 depicts the laser welding process arrangement. The sample under consideration comprised two sheets of brass and steel, measuring 50 mm × 20 mm with a thickness of 1.5 mm. Also, Table 1 illustrates the fundamental composition of S.S 308 and brass. The chemical composition of metals was performed by using Spark Emission Spectrometer method and the machine model SPECTROLAB S. For brass alloy, the CuZn39Pb3 is considered the equivalent alloy with this chemical composition.

For metallography analysis, the samples were polished with sand paper with grit size from 100 to 1500 under ASTME3 standard metallography preparation process. After final polishing, samples were etched via two etchants to reveal the cross sections of the dissimilar weld microstructure. For the brass base metal side, the welded samples were etched with a solution including 59 mg $FeCl_3$, 20 mL HCl, and 96 mL of C_2H_5OH. The stainless steel side was etched with a mixture of 30 mL of HCl, 10 mL of HNO_3 and 10 mL of $C_3H_8O_3$. After that, the microstructure of the etched samples was observed by optical microscope Olympus model GX-53.

3. Numerical simulation

The thermophysical characteristics of the two metals are critical in welding different materials. During cooling, a considerable difference in the thermal expansion and thermal diffusivity coefficients of neighboring metals produces tensile stress on one and compressive stress on the other. During welding, tensile stress metals might suffer hot cracking, whereas compressive stress metals may experience cold cracking during or after welding. In reality, stress concentrations are caused by changes in metal thermophysical characteristics.

Therefore, in this examination, it was tried to assess the temperature distribution and melting flow velocity during the welding procedure. Fig. 2 illustrates a view of the welding process and the position of the temperature history measurement. Because the heat distribution never reaches a stable state, and the cooling and heating rates are much higher than continuous laser welding. In pulsed laser welding, due to the small molten pool and rapid temperature changes occurring throughout the process in a short time, measurements of essential parameters, for example, temperature fields, velocity and rate of solidification, and thermal cycles, are complicated. These parameters are noteworthy because they determine the molten pool's shape, composition, and structure of the welded metal. Therefore, using the computational fluid dynamics (CFD) capabilities, this study simulated the pulsed laser welding method using the finite volume method. The numeric computation was performed utilizing the commercial computational fluid dynamics software Ansys Fluent 18. The user-defined functions (UDF) written in C language were used to obtain the source terms in the governing equations, boundary conditions, and variable thermophysical properties.

3.1. Modeling of laser welding process

Gaussian surface thermal flux and thermal source were utilized to model the absorbed energy from laser beam irradiation. Because in keyhole welding, the created plasma at the workpiece surface absorbs some of the energy. Additionally, based on the findings of Tlili et al. [38] research, it was determined that out of 6 possible thermal models, the cylindrical thermal model, and surface heat flux combination offers the most precise prediction in the numerical modeling process of keyhole welding. The following equations show the surface and volumetric thermal fluxes. The surface heat flux was considered the boundary condition, and the volumetric heat flux was considered the source term in the energy equation. [39–41].

$$q_s(x,y) = \frac{3f_1\eta p}{\pi r_s^2} exp\left(-3\frac{(x^2+y^2)}{r_s^2}\right) \quad (1)$$

$$q_v(x,y,z) = \frac{6f_2\eta p}{\pi r_v^2 d} exp\left(-3\frac{(x^2+y^2)}{r_v^2}\right)\left(\frac{mz+r_v}{md+2r_v}\right) \quad (2)$$

where q_s is the thermal flux, q_v is the heat source, p is power of laser, f_1, f_2 are the power distribution factors, d indicates the cylindrical heat's thermal source, r_s and r_v characterize the radius of the surface thermal flux and cylindrical heat source, η is the coefficient of absorption m is the damping factor of the heat source, which is estimated through different simulations [39].

Radius of heat flux and the heat source are determined according to the spot radius, and the thickness of the sheets was used to calculate the cylinder's height. Based on the findings of Ducharme et al. [42], f_1 and f_2 are primarily considered to be 0.25 and 0.75, respectively. m is determined by numbers of simulation. The damping coefficient is determined based on the wavelength and the absorption coefficient.

3.2. Governing equations

Keyhole laser welding entails the utilization of highly high beam intensity for material processing. This technique gives rise to the generation of metal vapor adjacent to the molten metal, resulting in the displacement of a portion of the melt and the creation of a vapor column

Table 2
Thermophysical characteristics of S.S 308 and brass [44–48].

Nomenclature	Symbol	Material	Value		Unit
Density of solid phase	ρ_s	*AISI 308*	$\rho_s = 8020 - 0.501(T - 298)$		$kg\,m^{-3}$
		Brass	$\rho_s = 8422 - 0.4985T$		
Density of liquid phase	ρ_l	*AISI 308*	$\rho_l = 6900 - 0.8(T - 1727)$		$kg\,m^{-3}$
		Brass	$\rho_l = 8432.9 - 0.9689T$		
Solidus temperature	T_s	*AISI 308*	*1673*		K
		Brass	*1173*		
Liquidus temperature	T_l	*AISI 308*	*1727*		K
		Brass	*1178*		
Ambient temperature	T_∞		*298*		K
Thermal conductivity	k	*AISI 308*	$k = 9.83 + 14.84 \times 10^{-3}T - 7.106 \times 10^{-7}T^2 k = 5.98 + 11.84 \times 10^{-3}T$	$298 \le T \le 1673 T > 1793$	$W\,m^{-1}K^{-1}$
		Brass	$k = 140.62 + 112.14 \times 10^{-4}Tk = 45.43 + 26 \times 10^{-3}T$	$T \le 1180 T > 1228$	
Specific heat	c	*AISI 308*	$c = 0.451 + 2.1 \times 10^{-4}T - 7.98 \times 10^{-10}T^2$	$298 \le T \le 1727$	$J\,g^{-1}K^{-1}$
		Brass	$c = 0.354 + 1.11 \times 10^{-4}T 0.489$	$T \le 1173 T > 1178$	
Melting latent heat	L_m	*AISI 308*	2.90×10^5		$J\,kg^{-1}$
		Brass	1.601×10^5		
Stefan-Boltzmann constant	σ		5.67×10^{-8}		$W\,m^{-2}K^{-4}$
Dynamic viscosity	μ		*0.0007*		$kg\,m^{-1}s^{-1}$

known as the keyhole. By directly imparting energy to the material while minimizing heat transfer, this approach optimizes weld depth. A cylindrical heat flux model was employed to accurately estimate the absorbed energy within the material. Consequently, the vapor column was disregarded and replaced with the cylindrical heat source. The following assumptions are used to derive the governing equations for the numerical laser welding simulation.

- Newtonian melt flow was considered incompressible and laminar.
- The initial temperature was assumed to 298 K.
- Plasma formed on the molten pool's surface was disregarded.

Continuity equation:

$$\nabla.(\rho\vec{U}) = 0 \tag{3}$$

Momentum equation:

$$\frac{\partial\left(\rho\vec{U}\right)}{\partial t} + \nabla.\left(\rho\vec{U}\vec{U}\right) = -\nabla p + \nabla.\left(\mu\nabla\vec{U}\right) + \rho\vec{g} - \frac{\mu}{K}\left(\vec{U}\right) \tag{4}$$

where K, μ, $\vec{g}$, p, $\vec{U}$, t, ρ are Darcy resistance coefficient, dynamic viscosity, gravity acceleration vector, pressure, velocity vector, time and density, respectively.

To ascertain the regions of melting and solidification, the liquid fraction was determined using the follow equation. During the solidification of the melt or the melting of the solid, the liquid fraction ranges between 0 and 1. Consequently, by incorporating the liquid fraction into the momentum equation, the force resulting from the alteration in material phase can be exerted [43]. The mushy zone constant, referred to as D, defines the material under investigation and measures the degree of coexistence between solid and liquid phases during solidification or melting processes. Equation 6 provides the liquid fraction, denoted as f_L. Also, c is a constant value.

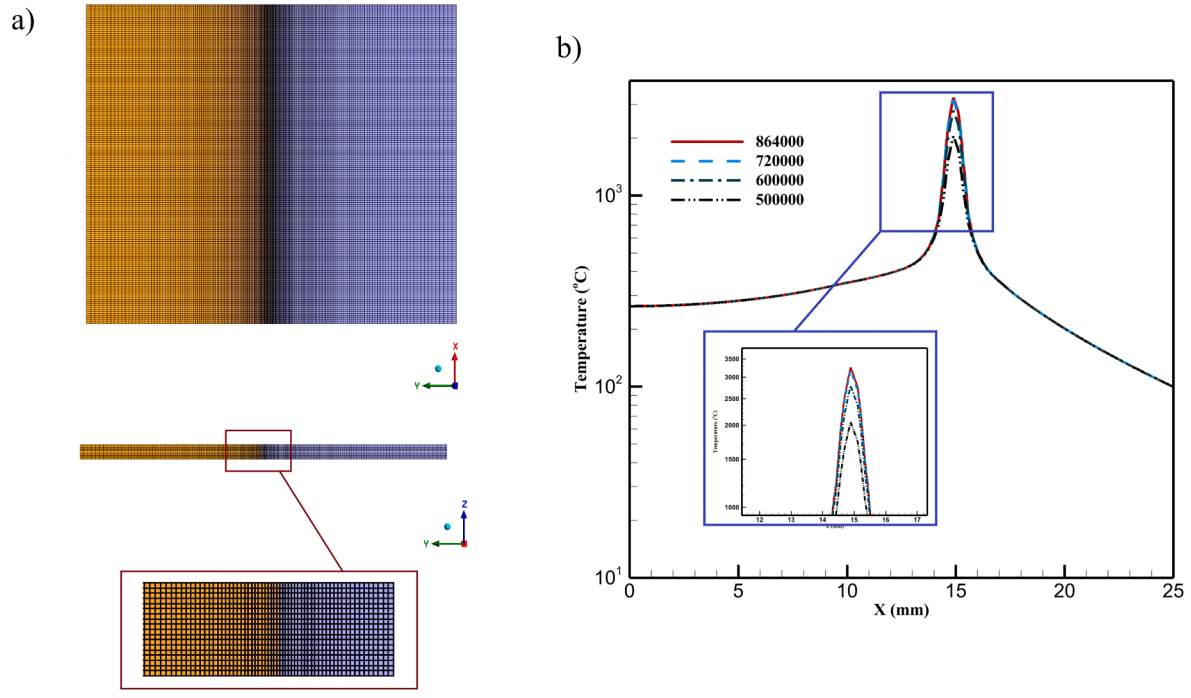

Fig. 3. (a) Structured grids, (b) Mesh independence study.

Table 3
Laser parameters.

Sample	Beam deviation (mm)	Welding Speed(cm/s)	Pulse Duration(ms)	Frequency(Hz)	Peak power(W)	Focal position(mm)
1	0	0.3	12	12	2500	0
2	+0.5	0.3	12	12	2500	0
3	−0.5	0.3	12	12	2500	0

$$K = \frac{f_L^3 + c}{D(1 - f_L)^2} \tag{5}$$

$$f_L = \begin{cases} 0 & T \le T_s \\ \dfrac{T - T_s}{T_l - T_s} & T_s < T < T_l \\ 1 & T \ge T_l \end{cases} \tag{6}$$

Energy equation:

$$\frac{\partial(\rho H)}{\partial t} + \nabla.\left(\rho \vec{U} H\right) = \nabla.(k\nabla T) + h(t) q_V \tag{7}$$

k is the thermal conductivity coefficient, H is the total enthalpy, T is the temperature and h (t) is the pulse laser welding factor.

3.3. Boundary conditions

The surface heat flow described in Equation (6) was used to specify the boundary condition at the surface of the sheets. Equations (7) and (8) describe shear stress on the workpiece's surface induced by the surface tension gradient, as well as the formation of Marangoni stream in the molten pool:

$$k\frac{\partial T}{\partial \vec{n}} = -\varepsilon\sigma\left(T^4 - T_\infty^4\right) - h(T - T_\infty) + h(t) q_S \tag{8}$$

$$\mu\frac{\partial u}{\partial z} = -\frac{\partial \gamma}{\partial T}\frac{\partial T}{\partial x} \tag{9}$$

$$\mu\frac{\partial v}{\partial z} = -\frac{\partial \gamma}{\partial T}\frac{\partial T}{\partial y} \tag{10}$$

where ε is the coefficient of emission, T_∞ is the temperature of surrounding, σ is the Stefan–Boltzmann coefficient, h is the convection heat transfer coefficient, and γ is the surface tension.

The thermal boundary condition considered in the lateral and lower surfaces includes the convection and thermal radiation to the surrounding (Equation 11):

$$k\frac{\partial T}{\partial \vec{n}} = -\varepsilon\sigma\left(T^4 - T_\infty^4\right) - h(T - T_\infty) \tag{11}$$

3.4. Thermophysical properties

Table 2 depicts the thermophysical attributes of S.S 308 and brass alloy at 298 K. As an outcome of the high-temperature alterations during the laser welding, the temperature variable thermophysical characteristics were determined.

3.5. Computational domain

To accurately apply the heat flux when the moving heat source passes through the welding region at specific time steps, fine meshes were selected. These regions are expected to have the most severe temperature gradients. On the other hand, regions further away from the weld were meshed with a coarse mesh. Fig. 3.a displays the symmetrical graded mesh in three dimensions for the plates. To assess the independence of the grid, four computing grids were juxtaposed. Fig. 3.b illustrates the alterations in temperature at the intersection of two components and on the plate surfaces. The laser parameters' outcomes encompass a maximum power of 2500 W, pulse width of 12 ms, speed of 3 mm/s, frequency of 12 Hz, and offset of 0 mm. It is evident that there is no substantial variation in the results between the computational domain with 720,000 elements and that with 864,000 pieces. Consequently, the 720,000 elements were selected for the intended geometry. Additionally, the time step was established by the variable pulse width and frequency. This procedure decreased the computational cost and met the convergence requirement of 10^{-4}.

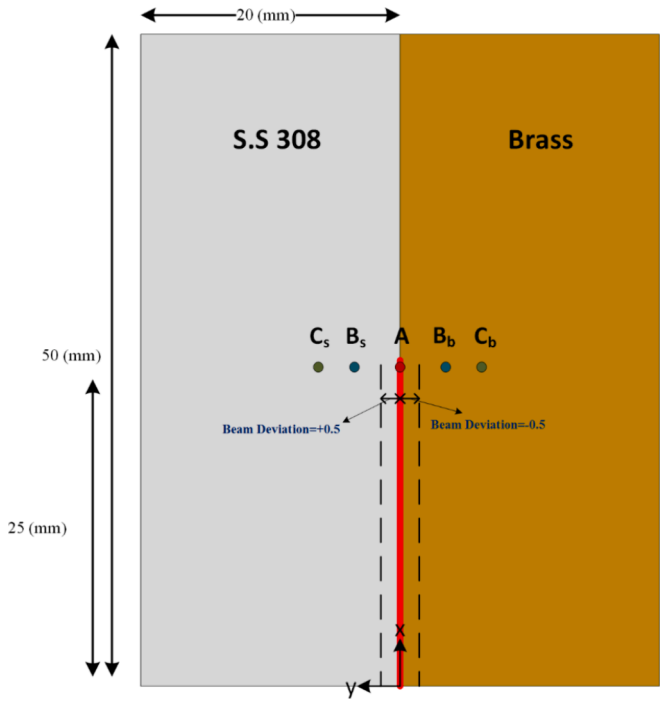

Fig. 4. Specified points to investigate of temperature changes versus time.

The enthalpy-porosity technique was employed to replicate the melting and solidification process in pulsed laser welding. In this method, the boundary between the solid and melted states is not accurately monitored. The liquid fraction, which quantifies the proportion of the volume occupied by cells in a liquid condition throughout the whole computational domain, is defined. The liquid fraction in each iteration is determined by the enthalpy balance. The SIMPLE algorithm was employed to link the velocity and pressure fields. The convergence accuracy for all equations was set to 10^{-4}. To simulate pulsed laser welding using the finite volume approach, the energy equation and the boundary condition on the surface of the sheets were modified to include a parameter called h (t). The value of h was calculated based on the pulse width and frequency over time. When the pulse is active, the value of h (t) is 1, and when the pulse is inactive, h (t) is 0. In order to eliminate any dependence on the time step, a time step value of 10^{-4} was used.

4. Results and discussions

To assess the influence of laser beam variation on temperature distribution and melt flow, three different modes of laser beam placement

Table 4
Coordinates of specified points to investigate the temperature changes versus time.

	x(mm)	y(mm)	z(mm)
A	25	0	1.5
B_b	25	−1	1.5
C_b	25	−2	1.5
B_s	25	+1	1.5
C_s	25	+2	1.5

were considered, shown in Table 3. Fig. 4 and Table 4 show the locations considered to examine the time history of temperature.

4.1. Temperature distribution

The topic at hand pertains to the study of temperature behavior and heat transfer mechanisms in the context of material processing, manufacturing, and welding. As shown in Fig. 5, analyzing the temperature history at the junction position of two workpieces (point A) for different beam deviations is an essential phase in improving the quality of welded connections. The graph clearly demonstrates that when the laser beam is aimed toward the joint, the temperature reaches its highest value, which effectively influences the quality of the welded connection. An intriguing finding from this study is that the temperature fluctuations are more significant when the beam deviation is −0.5 mm owing to the high thermal diffusivity of brass. This observation highlights the importance of considering material properties when analyzing the welded junction's temperature behavior. Furthermore, the data presented in Fig. 6 highlights a distinct temperature behavior between brass and S.S 308, which can be attributed to their differing conductive heat transfer coefficients. The higher conductive heat transfer coefficient of brass results in a higher temperature at the joint location of two

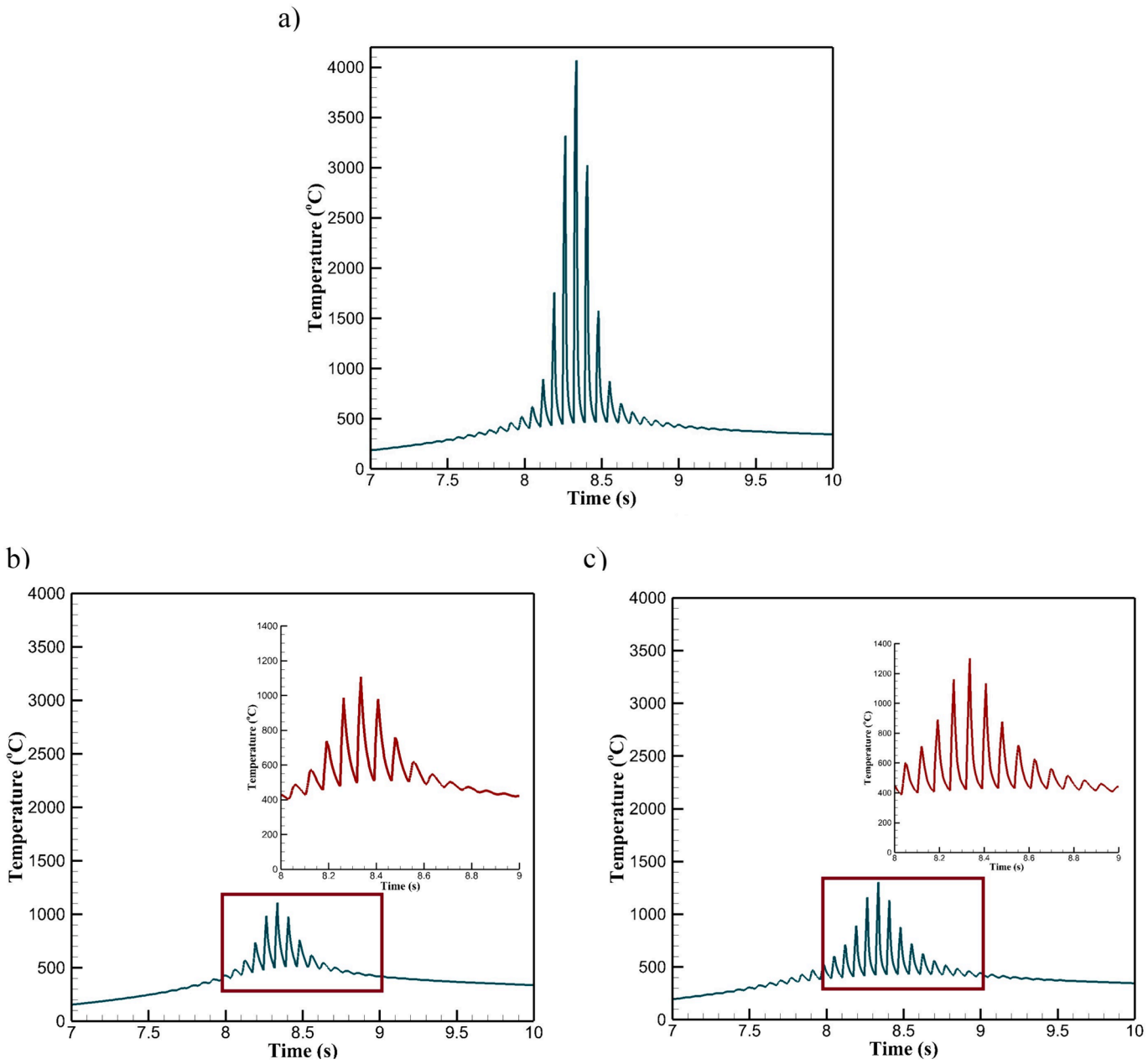

Fig. 5. Temperature history from the numerical simulation at the joint location (point A) of two workpieces, (a) beam deviation = 0 mm, (b) beam deviation=+0.5 mm (S.S 308), and (c) beam deviation = −0.5 mm (brass).

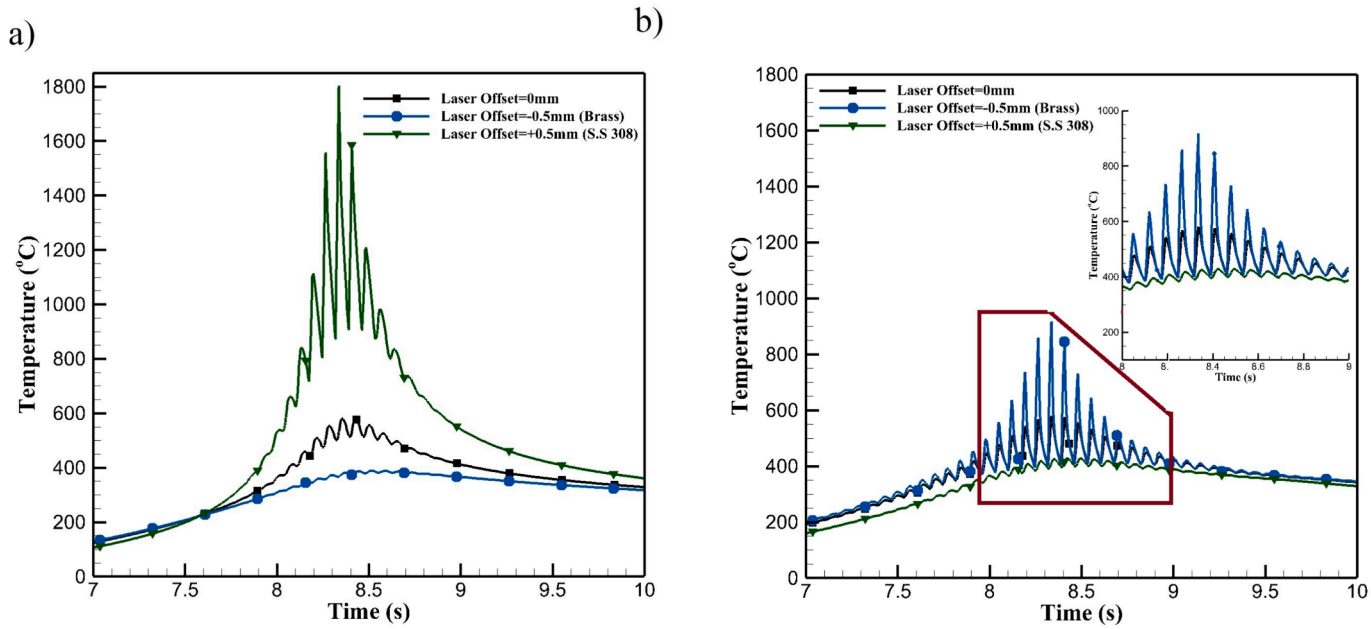

Fig. 6. Temperature history from the numerical simulation at 1 mm from the junction (point B) of two workpieces, (a) S.S 308 (B_s) and (b) brass (B_b).

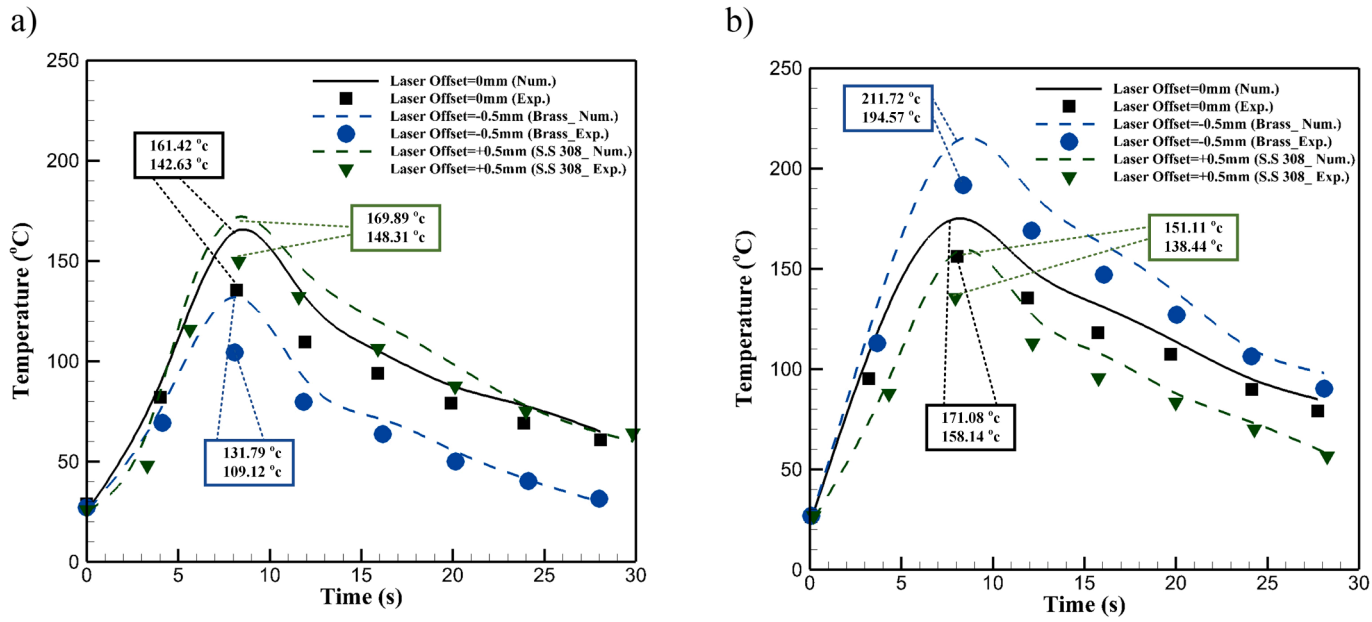

Fig. 7. Comparison of temperature history for numerical and experimental results at a 2 mm distance from the joint location of two workpieces, (a) S.S 308 (C_s) and (b) brass (C_b).

workpieces in contrast to S.S 308.

The fusion point of brass is a crucial element in temperature behavior. The low melting temperature of brass leads to the increased role of convection heat transfer, which results in the transfer of heat through fluid motion. The phenomenon is responsible for the higher temperature of brass than S.S 308 at a distance of 1 mm from the joint position of two workpieces (point B) for a 0 mm deviation, as shown in Fig. 5. These findings demonstrate the significance of considering material properties and heat transfer mechanisms when analyzing the temperature behavior of welded joints. This approach can lead to improvements in the quality of the welding process. The temperature history at different locations and situations clearly reflect the resultant interactions of all phenomena took place during welding process. In case the laser beam deviated toward the brass alloy, the melting volume of brass and thereby general melt volume of fusion zone including stainless steel increased and therefore the temperature significantly increased. On the other hand, by laser irradiating toward brass, the absorbsion rate of brass due to receiving higher level of energy, remarkably increased and as a result the melting efficiency of brass improved. Therefore, it could be said that the laser material interaction in terms of thermophysical properties can play an important role to evaluate the weld condition through measuring the temperature during laser welding.

Given that the temperature history record is situated at the location of 25 mm away from the starting point of the piece (it takes 8.33 s for the laser beam to reach this point). Moreover, the temperature distribution in pulse laser welding is not just determined by the laser process input parameters, but also influenced by factors such as the thermal diffusion coefficient, thermal conductivity coefficient, and distinct

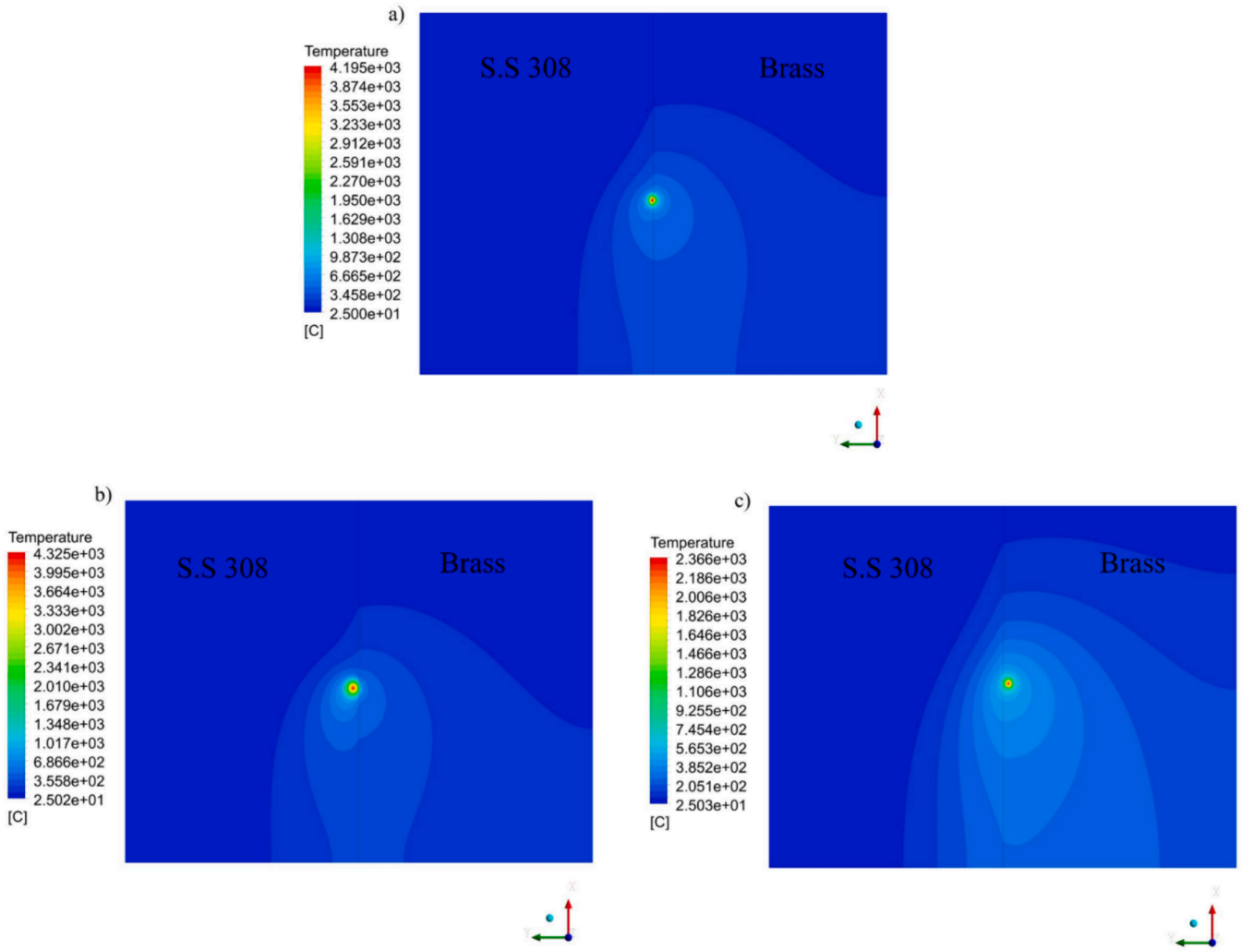

Fig. 8. Distribution of temperatures on the workpiece's surface, a) beam deviation = 0 mm, b) beam deviation=+0.5 mm (S.S 308) and c) beam deviation = −0.5 mm (brass).

thermophysical properties of the two metals. Figs. 5 and 6 are merely a response to the temperature value at varying transverse distances of 25 mm from the starting point of the parts. Consequently, the temperature peaks fluctuation is distinct from the input laser frequency of 12 Hz.

Fig. 7 illustrates a comparison of numerical simulation outcomes and experimental results. This figure shows that the modeling of received energy from the laser beam was done with appropriate accuracy; the numerical and experimental outcomes correspond well. Although brass has a very low absorption coefficient compared to S.S 308, by comparing Fig. 7.a and 7.b, it can be seen that in the beam deviation of 0 mm, the temperature in the brass workpiece was higher than that of S.S 308. It was due to the increase in the size of the molten pool, which occurred in the brass workpiece. The thermocouple and data recorder used in this experiment had limitations that made detecting temperature only every 2.5 s possible. Consequently, only the temperatures measured at these exact time points were used to draw the graph to ensure proper comparison between the numerical and experimental data. Even so, it is clear that the trend of temperature changes over time is consistent. The dimensions of the molten pool derived from the outcomes of the numerical simulation and experimental investigation were compared to validate more precisely.

The temperature contour in Fig. 8 at time 5 s illustrates the impact of various laser beam variations on the temperature field. The thermal diffusivity coefficient of brass and S.S 308 at 100 °C is about 36.5 and 4 mm^2/s, respectively. This difference in coefficient led to an increase in temperature and heat-affected zone in S.S 308 compared to brass. The maximum temperature significantly decreased while the laser beam was 0.5 mm away from the brass workpiece. This can be attributed to the low absorption coefficient and increased conduction heat transfer. Consequently, the laser beam deviation substantially impacted temperature distribution and heat transfer, emphasizing the necessity of accuracy in laser processing.

4.2. *Melting flow*

The surface tension differential at the liquid metal's surface causes the production of a Marangoni flow at the melt flow's surface. The slope of surface tension variations versus temperature, determines the direction of melt flow and flow velocity. With a negative Marangoni coefficient, the surface tension drops with enhancing temperature, causing the melt to shift from the region of high temperature to the mushy region. The Marangoni effect generally known as is a mass transfer phenomenon that fluid transferred from low surface tension areas to higher surface tension areas [28]. A positive surface tension gradient generally leads to a radial inward flow and thereby leading to a deep and narrower melt-pool. The melt-pool fluid flow is dominated by the Marangoni convection effect caused by the surface tension gradient although other physical phenomena including recoil pressure and buoyancy force have less impact on melt-pool fluid flow [49].

Fig. 9 depicts the velocity vector and form of the molten pool

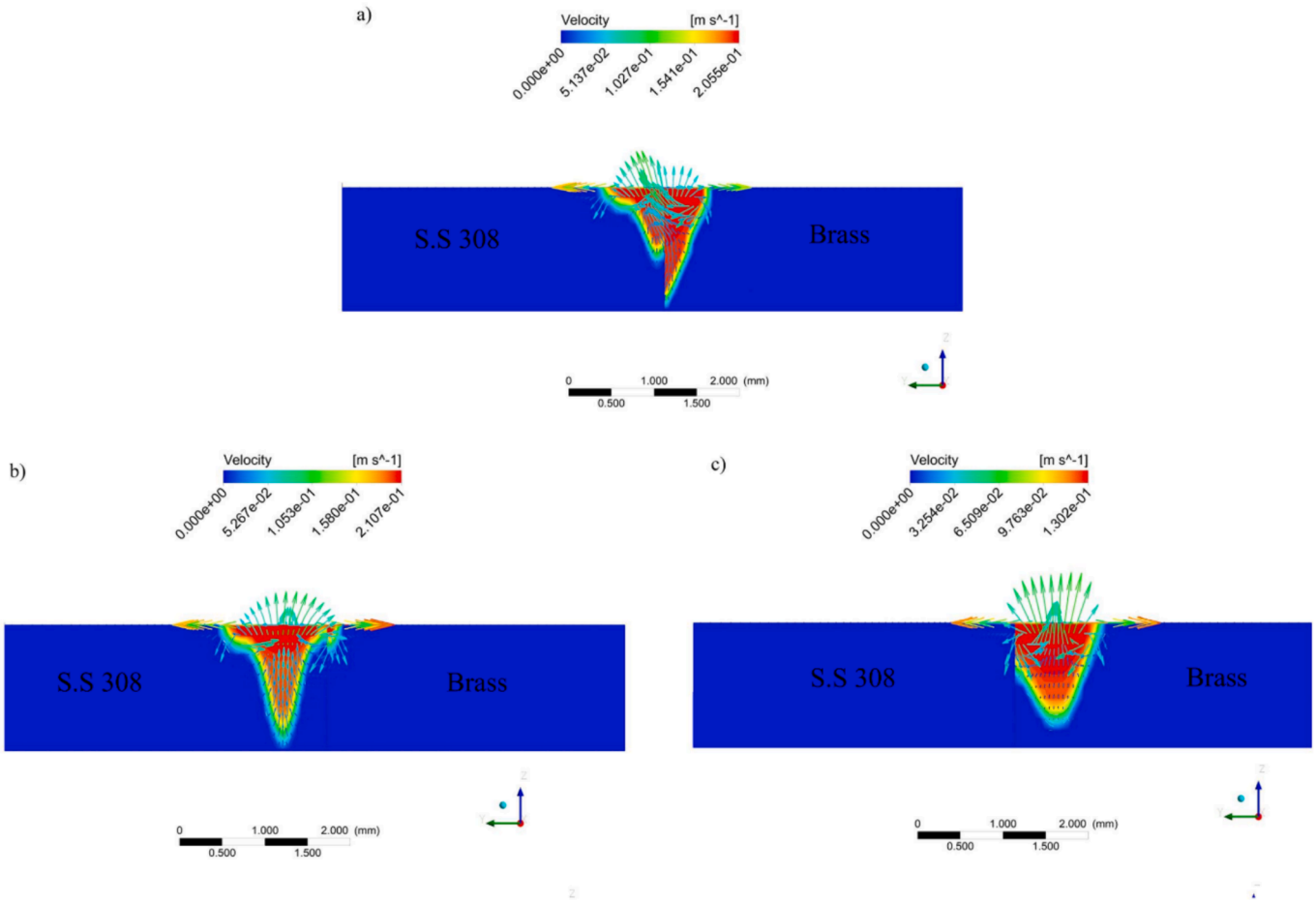

Fig. 9. Melting flow and velocity vector at the workpiece's cross section, (a) beam deviation = 0 mm, (b) beam deviation=+0.5 mm (S.S 308) and (c) beam deviation = −0.5 mm (brass).

depending on the laser beam deviations. Due to the fact that the slope of surface tension variations versus temperature and temperature gradient in S.S 308 is higher than that of brass, this factor leads to the movement of melt flow towards the S.S 308. According to Fig. 9. a, further melt volume formed in the brass workpiece because of the low melting temperature, whereas when the beam of the laser was shifted to the brass workpiece by 0.5 mm, only the brass sheet was melted and A small amount of melt was created in S.S 308 since to the brass alloy's low absorption coefficient and high thermal conductivity coefficient.

As shown in Fig. 10, the velocity vector and the weld bead extension and shape were presented to clarify the numerical simulation results. In case the laser beam adjusted about 0.5 mm toward S.S 308, because of the higher temperature gradient and more absorption coefficient of SS. 308, more melt volume was observed to create melt pool and weld bead. Fig. 10b implies that the higher temperature gradient and melt volume were created on the S.S 308 side. Furthermore, Fig. 10b shows the actual weld bead surface of the weld to compare the simulation results with experiments. Due to having a higher melting temperature and low coefficient of thermal conductivity of S.S 308, a higher melting volume was observed on the S.S 308 side. On the other hand, it could be said that the high thermal conductivity of brass limits the extension of S.S 308 melting toward the brass side. In this case, it can be concluded that only partial melting of the brass through the heat transfer mechanism was the predominant factor in creating the joint between brass and S.S 308. When the laser beam deviated toward S.S 308 due to the high reflectivity of brass, no clear melt volume was created directly through laser beam absorption. The main silver color texture of the weld bead surface and the higher weld bead width of S.S 308 confirm this phenomenon. Fig. 10a illustrates the melt velocity and melt pool extension numerically and experimentally orderly. In case the laser beam irradiated the center of the junction, more brass melting volume was created due to having some reasons. The lower melting point of brass and higher thermal conductivity created a higher volume of molten metal toward the brass. Although the brass has a lower absorption rate but, melted brass has higher absorbing rate in comparison to solid state. Hence, the melted volume of brass increased according to the higher absorption rate of brass at the liquid phase during the welding process. Another factor limiting the extension of the weld bead at the S.S 308 side would be the high thermal conductivity of brass which decreases S.S 308 melting volume. It can be concluded that the brass melting participation rate has been clearly more than S.S 308 to form a melt joint.

When the laser beam shifted 0.5 mm to the brass side, the major part of melt volume was created on the brass side. Fig. 10c depicts the melt volume on the brass side, while no clear melting was observed on the S.S 308 side. Fig. 10c shows the actual welded sample, which indicates no clear S.S 308 melting. Low laser beam absorption of the brass alloy, irradiation of the main part of laser beam energy to the brass alloy, and thereby high thermal conductivity coefficient of that would limit S.S 308 melting. Apart from these, the lower melting point of the brass could not overcome to melt the S.S 308 through heat conduction. As shown in Fig. 10c, only a thin layer of melted brass has been covered the top surface of the S.S 308 side because of the effect of evaporation of ZN element during the laser welding process.

Fig. 11 illustrates the comparison between the morphology of the molten pool generated through numerical and experimental analysis on the cross-section of two components with varying beam offsets. It is

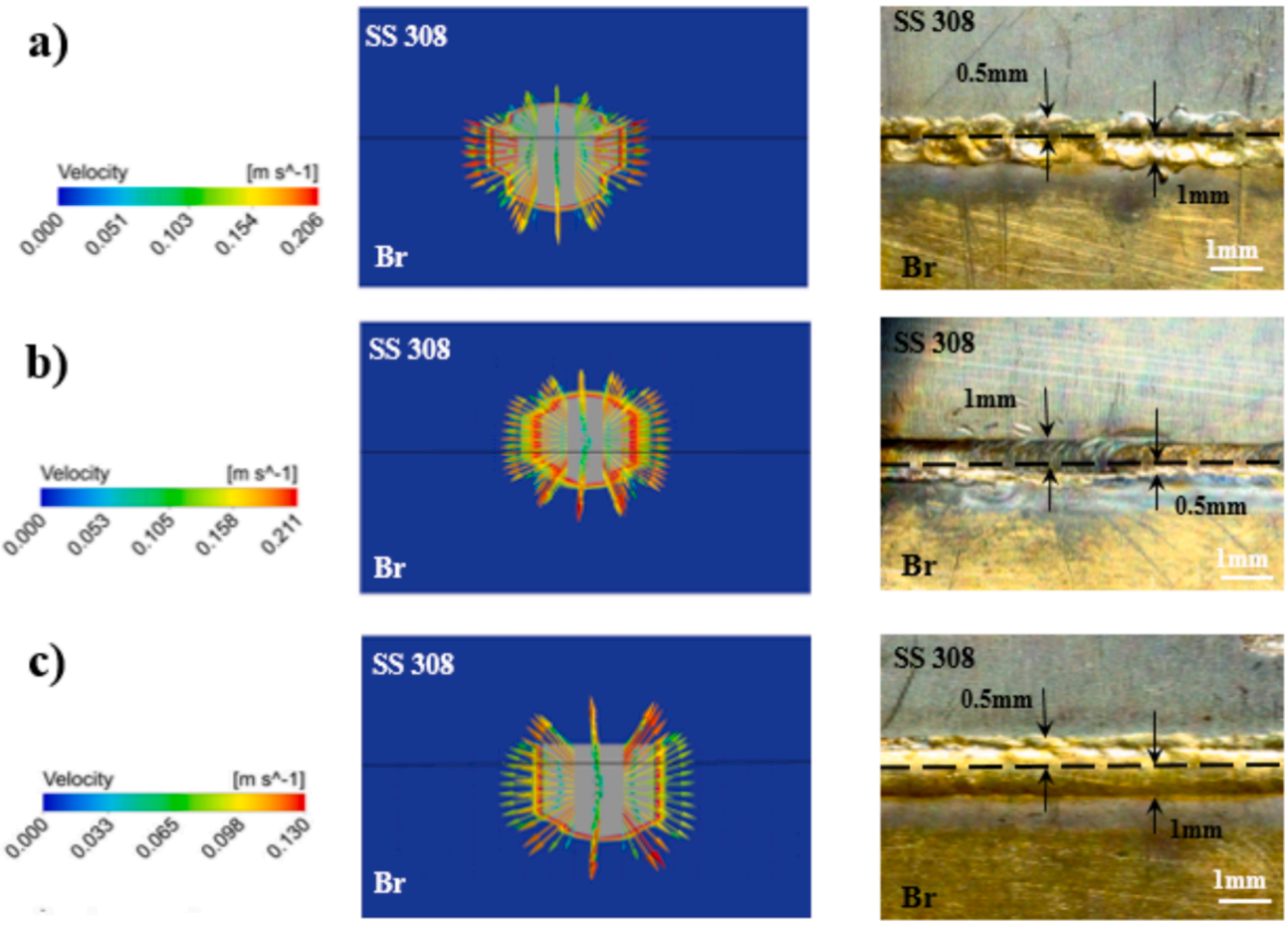

Fig. 10. Comparison of the numerical and experimental results of melt flow and bead shape formation: (a) beam deviation = 0 mm, (b) beam deviation=+0.5 mm (S. S 308) and (c) beam deviation = −0.5 mm (brass).

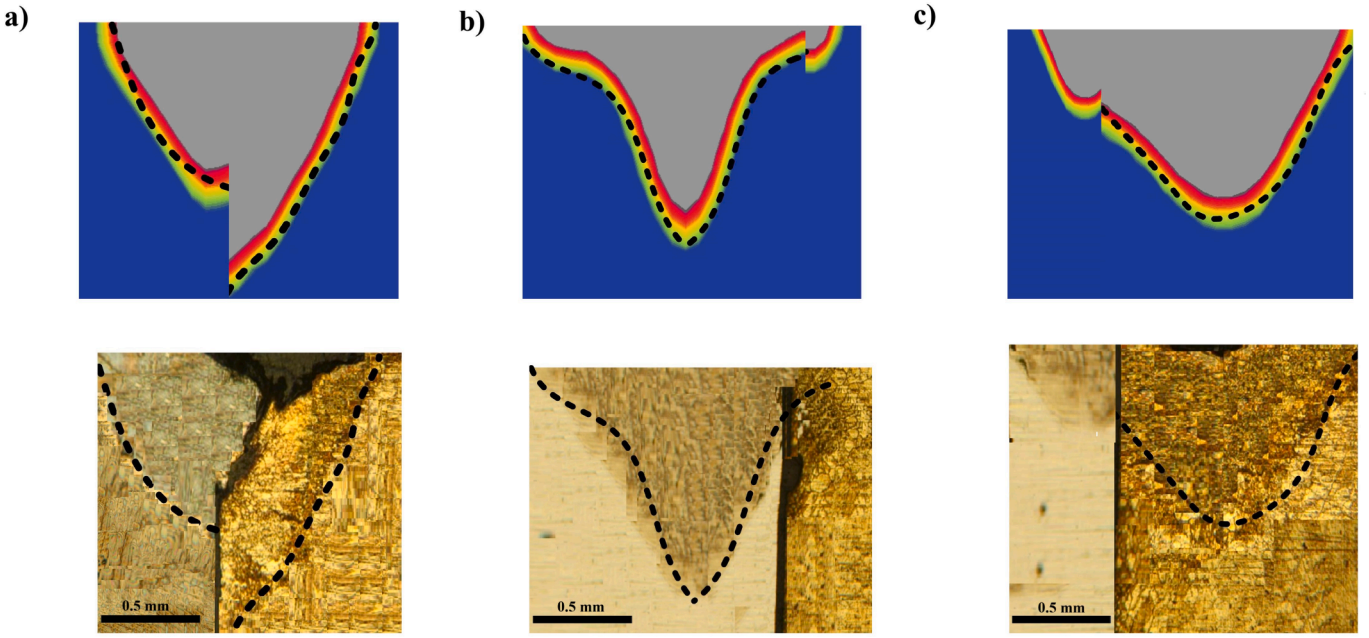

Fig. 11. Comparison of numerical and experimental bead shape formation in the cross-sectional (a) beam deviation = 0 mm, (b) beam deviation=+0.5 mm (S.S 308), and (c) beam deviation = −0.5 mm (brass).

Table 5
Comparison of the maximum depth of the molten pool obtained from numerical simulation with experimental results.

Sample	Numerical simulation results (mm)	Differences with experimental results (%)
1	1.162	3.17
2	0.917	3.95
3	0.809	4.23

evident that the numerical findings exhibit a satisfactory concurrence with the dimensions of the molten pool acquired from the experimental investigation, thereby affirming the accurate application of thermal models and governing equations pertaining to this investigation. Additionally, Table 5 presents the maximum depth of melt penetration in both components, revealing that the most significant discrepancy, associated with an offset of −0.5 mm (brass), amounted to 4.23 %.

In other study, the effect of different process parameters on the temperature field in laser welding of H62 brass was investigated using finite elements methods to study the influence of different process parameters on the temperature field. The molecular dynamics method was used to analyze the formation process of the weld from the atomic scale. Finally, no obvious defects through suitable combinations of different process parameters were observed [50]. In comparison to their study, dissimilar laser welding simulation results can effectively predict both the temperature field variation and melting efficiency of both metals related to laser welding process parameters.

Laser dissimilar welding of titanium and brass alloy foils was investigated via laser experiments and smoothed particle hydrodynamics (SPH) simulation. The results illustrate that the Ti/brass interfaces under different laser energies were ring-shaped, and the increase in laser energy resulted in the increase in effective welding area along the welding direction [51]. A clear comparison with their study implies that by deviating laser beam maximum energy toward brass alloy, the volume of melted material significantly increased on width of the weld bead while deviating laser beam toward stainless steel increased the melted volume through depth of penetration.

Laser welding-brazing of 5052 aluminum alloy and H62 brass with Zn-15 %Al filler was developed in butt configuration. The welding deviation impact on microstructural and mechanical characteristics depicts different microstructure and tensile strength during welding [52]. An evident comparison between stainless steel/ brass shows different contribution of alloy and melt pool geometry which directly influenced the joint microstructure and mechanical properties.

5. Conclusions

The influence of laser beam variation on temperature and melt flow distribution in pulsed laser welding of two heterogeneous metals, brass, and S.S 308, was examined using the finite volume approach and experimental study. The energy absorbed by the laser beam was modeled using a Gaussian distribution. The simulation and experimental investigation yielded the following results:

- The maximum temperature was higher than the other conditions when the laser beam was 0.5 mm on the 308 stainless steel sheets.
- A Marangoni flow formed due to a negative surface tension gradient and buoyancy force in the molten pool.
- As compared to stainless steel, the low melting point of brass alloy contributed to an enhancement in the volume of the molten pool in the deviation of 0.0 mm beam.
- The velocity of the melt flow increased by 0.0102 m/s when the laser beam deviated towards the S.S 308 sheet due to an increase in temperature gradient and shear stress.
- The numerical simulation agreed well with the experimental findings.

6. Code availability

Not applicable.

Ethics approval

Not applicable.

8. Consent to participate

Not applicable.

9. Consent for publication

Not applicable.

CRediT authorship contribution statement

Jie Zhang: Software, Supervision, Writing – review & editing. **Mohammad Hossein Razavi Dehkordi:** Resources, Formal analysis, Conceptualization. **Mohammad Javad Kholoud:** Writing – review & editing, Writing – original draft, Software. **Hamidreza Azimy:** Writing – original draft, Supervision, Resources. **Saeed Daneshmand:** Methodology, Investigation, Formal analysis.

Declaration of competing interest

The authors declare that they have no known competing financial interests or personal relationships that could have appeared to influence the work reported in this paper.

Data availability

The raw/processed data required to reproduce these findings cannot be shared at this time due to technical or time limitations.

References

[1] J. Wang, Z. Sun, L. Gu, H. Azimy, Investigating the effect of laser cutting parameters on the cut quality of Inconel 625 using Response Surface Method (RSM), Infrared Phys. Technol. 118 (2021) 103866.
[2] H. Taherdoost, M. Madanchian, Analytic Network Process (ANP) method: A comprehensive review of applications, advantages, and limitations, J. Data Sci. Intell. Syst. (2023), https://doi.org/10.47852/bonviewJDSIS3202885.
[3] M.H. Dehkordi, D.J. Jasim, A.H. Al-Rubaye, M. Akbari, S.A. Bagherzadeh, M. Ghazi, H. Mohammadkarimi, Modeling and multiobjective optimization of thermal effects of fiber laser cutting of Inconel 600 sheet by employing the ANN and multi-objective PSO algorithm, J. Laser Appl. 35 (4) (2023 Nov 1).
[4] L.I.U. Xiuru, W.U. Xia, C.H.E.N. Dajun, et al., Microstructure and mechanical properties of thin aluminum alloy by friction stir welding, J. Ordnance Equipment Eng. 44 (11) (2023) 229–234.
[5] B. Peng, et al., 3D-STCNN: Spatiotemporal Convolutional Neural Network based on EEG 3D features for detecting driving fatigue, J. Data Sci. Intell. Syst. (2023), https://doi.org/10.47852/bonviewJDSIS3202983.
[6] J. Li, T. Sui, X. Dong, F. Gu, N. Su, J. Liu, C. Xu, Large eddy simulation studies of two-phase flow characteristics in the abrasive flow machining of complex flow ways with a cross-section of cycloidal lobes, Int. J. Hydromechatronics 5 (2) (2022) 136–166.
[7] M.I.A.O. Guanghong, M.A. Qiuyue, H.U. Yu, et al., Numerical simulation of thermal explosion welding of tungsten copper bimetallic plates, J. Ordnance Equipment Eng. 44 (8) (2023) 257–265.
[8] N. Luo, et al., Fuzzy logic and neural network-based risk assessment model for import and export enterprises: A review, J. Data Sci. Intell. Syst. (2023), https://doi.org/10.47852/bonviewJDSIS32021078.
[9] J. Zhao, Z. Wang, Y. Han, Stability analysis of elastic steel beam-column under high temperature, Int. J. Hydromechatronics 5 (1) (2022) 44–79.
[10] A.R. Miandoab, S.A. Bagherzadeh, A.H. Isfahani, Numerical study of the effects of twisted-tape inserts on heat transfer parameters and pressure drop across a tube carrying Graphene Oxide nanofluid: An optimization by implementation of Artificial Neural Network and Genetic Algorithm, Eng. Anal. Bound. Elem. 1 (140) (2022 Jul) 1.
[11] Y. Zhang, M.H.R. Dehkordi, M.J. Kholoud, H. Azimy, Z. Li, M. Akbari, Numerical modeling of the temperature distribution and melt flow in dissimilar fiber laser

welding of duplex stainless steel 2205 and low alloy steel, Opt. Laser Technol. 174 (2024) 110575.
[12] L. Wang, Y. Rong, Review on processing stability, weld defects, finite element analysis, and field assisted welding of ultra-high-power laser (≥ 10 kW) welding, Int. J. Hydromechatronics 5 (2) (2022) 167–190.
[13] L.I. Luyao, R.E.N. Luying, Y.A.N. Zhaoming, et al., Effects of heat treatment processing on microstructure evolution and microhardness of deformed Mg Gd Y Zn Zr Alloys, J. Ordnance Equipment Eng. 44 (10) (2023) 72–77.
[14] Y. Yongbin, S.A. Bagherzadeh, H. Azimy, M. Akbari, A. Karimipour, Comparison of the artificial neural network model prediction and the experimental results for cutting region temperature and surface roughness in laser cutting of AL6061T6 alloy, Infrared Phys. Technol. 108 (2020) 103364.
[15] M.J.H. Rawa, M.H. Razavi Dehkordi, M.J. Kholoud, N.H. Abu-Hamdeh, H. Azimy, Using the numerical simulation and artificial neural network (ANN) to evaluate temperature distribution in pulsed laser welding of different alloys, Eng. Appl. Artif. Intel. 126 (2023) 107025.
[16] M. Azari, E. Rasti, M.H.R. Dehkordi, H. Azimy, A. Zarei, S.A. Bagherzadeh, Investigation of temperature distribution and melt pool microstructure in laser fusion welding of Inconel 625 superalloy, J. Laser Appl. 33 (2) (2021) 022015.
[17] M.S. Khan, M.H. Razmpoosh, E. Biro, Y. Zhou, A review on the laser welding of coated 22MnB5 press-hardened steel and its impact on the production of tailor-welded blanks, Sci. Technol. Weld. Joining 25 (6) (2020) 447–467.
[18] Z. Liu, X. Jin, J. Li, Z. Hao, J. Zhang, Numerical simulation and experimental analysis on the deformation and residual stress in trailing ultrasonic vibration assisted laser welding, Adv. Eng. Softw. 172 (2022) 103200.
[19] J. Khan, E. Lee, K. Kim, A higher prediction accuracy–based alpha–beta filter algorithm using the feedforward artificial neural network, CAAI Trans. Intell. Technol. (2022), https://doi.org/10.1049/cit2.12148.
[20] T. Tyagi, S. Kumar, A.K. Malik, V. Vashisth, A Novel Neuro-Optimization Technique for Inventory Models in Manufacturing Sectors, *J. Comput. Cognitive* Eng. (2022).
[21] Z. Chen, Research on Internet Security Situation Awareness Prediction Technology Based on Improved RBF Neural Network Algorithm, *J. Comput. Cognitive* Eng. 1 (3) (2022) 103–108.
[22] Z. Li, S. Li, Recursive recurrent neural network: A novel model for manipulator control with different levels of physical constraints, CAAI Trans. Intell. Technol. (2022), https://doi.org/10.1049/cit2.12125.
[23] G. Krishna Kumar, C. Velmurugan, T. Kannan, Using the RSM method of improving process parameters of welding AISI 316 and nickel 201 using CO2 laser.
[24] M. Barma, U.M. Modibbo, Multiobjective Mathematical Optimization Model for Municipal Solid Waste Management with Economic Analysis of Reuse/Recycling Recovered Waste Materials, *J. Comput. Cognitive* Eng. 1 (3) (2022) 122–137.
[25] Y.-Q. Wang, J.-Y. Li, C.-H. Chen, J. Zhang, Z.-H. Zhan, Scale adaptive fitness evaluation-based particle swarm optimisation for hyperparameter and architecture optimisation in neural networks and deep learning, CAAI Trans. Intell. Technol. (2022), https://doi.org/10.1049/cit2.12106.
[26] C. Sun, M.H.R. Dehkordi, M.J. Kholoud, H. Azimy, Z. Li, Systematic evaluation of pulsed laser parameters effect on temperature distribution in dissimilar laser welding: A numerical simulation and artificial neural network, Opt. Laser Technol. 163 (2023) 109407.
[27] J.P. Oliveira, et al., Dissimilar laser welding of a CoCrFeMnNi high entropy alloy to 316 stainless steel, Scr. Mater. 206 (2022) 114219.
[28] S. Yan, Z. Meng, B. Chen, C. Tan, X. Song, G. Wang, Prediction of temperature field and residual stress of oscillation laser welding of 316LN stainless steel, Opt. Laser Technol. 145 (2022) 107493.
[29] A. Evdokimov, N. Doynov, R. Ossenbrink, A. Obrosov, S. Weiß, V. Michailov, Thermomechanical laser welding simulation of dissimilar steel-aluminum overlap joints, Int. J. Mech. Sci. 190 (2021) 106019.
[30] Y. Jin, et al., Effect of heat input on interfacial microstructure, tensile and bending properties of dissimilar Al/steel lap joints by laser Welding-brazing, Opt. Laser Technol. 142 (2021) 107218.
[31] H. Ding, J. Ma, C. Zhao, D. Zhao, Effect of welding speed, pulse frequency, and pulse width on the weld shape and temperature distribution in dissimilar laser welding of stainless steel 308 and brass alloy, J. Laser Appl. 33 (2) (2021) 022009.
[32] Y. Huang, et al., Optimization of weld strength for laser welding of steel to PMMA using Taguchi design method, Opt. Laser Technol. 136 (2021) 106726.
[33] J. Xin, et al., The microstructures and mechanical properties of dissimilar laser welding of copper and 316L stainless steel with Ni interlayer, Cryogenics 118 (2021) 103344.
[34] H. Xia, W. Tao, L. Li, C. Tan, K. Zhang, N. Ma, Effect of laser beam models on laser welding–brazing Al to steel, Opt. Laser Technol. 122 (2020) 105845.
[35] M. Ragavendran, M. Vasudevan, Laser and hybrid laser welding of type 316L(N) austenitic stainless steel plates, Mater. Manuf. Process. 35 (8) (2020) 922–934.
[36] K. Pańcikiewicz, A. Świerczyńska, P. Hućko, M. Tumidajewicz, Laser Dissimilar Welding of AISI 430F and AISI 304 Stainless Steels, *Materials* 13(20). doi: 10.3390/ma13204540.
[37] A. Sadeghian, N. Iqbal, A review on dissimilar laser welding of steel-copper, steel-aluminum, aluminum-copper, and steel-nickel for electric vehicle battery manufacturing, Opt. Laser Technol. 146 (2022.) 107595.
[38] I. Tlili, D. Baleanu, S. Mohammad Sajadi, F. Ghaemi, M.A. Fagiry, Numerical and experimental analysis of temperature distribution and melt flow in fiber laser welding of Inconel 625, Int. J. Adv. Manuf. Technol. 121 (1–2) (2022) 765–784.
[39] M.J. Kholoud, M. Akbari, Numerical investigation of molten pool dimension, temperature field and melting flow during pulsed laser welding of Ti-6Al-4V alloy sheets with different thicknesses, J. Laser Appl. 33 (3) (2021) 032012.
[40] Y. Ai, P. Jiang, C. Wang, G. Mi, S. Geng, Experimental and numerical analysis of molten pool and keyhole profile during high-power deep-penetration laser welding, Int. J. Heat Mass Transf. 126 (2018) 779–789.
[41] P. Xia, et al., Prediction of weld shape for fiber laser keyhole welding based on finite element analysis, Int. J. Adv. Manuf. Technol. 75 (1) (2014) 363–372.
[42] R. Ducharme, P. Kapadia, J. Dowden, A mathematical model of the defocusing of laser light above a workpiece in laser material processing, in: International Congress on Applications of Lasers & Electro-Optics, AIP Publishing, 1992, pp. 187–197.
[43] J.G. Berryman, S.C. Blair, Kozeny–Carman relations and image processing methods for estimating Darcy's constant, J. Appl. Phys. 62 (6) (1987) 2221–2228.
[44] K.C. Mills, Recommended Values of Thermophysical Properties for Selected Commercial Alloys, Woodhead, 2002.
[45] Z. Zhang, P. Farahmand, R. Kovacevic, Laser cladding of 420 stainless steel with molybdenum on mild steel A36 by a high power direct diode laser, Mater. Des. 109 (2016) 686–699.
[46] R.D. Pehlke, A. Jeyarajan, H. Wada, Summary of thermal properties for casting alloys and mold materials, NASA STI/Recon Technical Report N 83 (1982) 36293.
[47] G. Grimvall, Thermophysical Properties of Materials, Elsevier, 1999.
[48] J.J. Valencia, P. Quested, Thermophysical properties, *Modeling Casting Solidification Process.* 189 (2001).
[49] T.-N. Le, Y.-L. Lo, Effects of sulfur concentration and Marangoni convection on melt-pool formation in transition mode of selective laser melting process, Mater. Des. 179 (2019) 107866.
[50] W. Tang, Y. Huang, X. Wang, H.a. Ming, Z. Liu, X. Wang, An investigation on microstructure and mechanical properties of H62 brass thin-sheet by fiber laser welding: Experiments and multi-scale simulations, Opt. Laser Technol. 171 (April 2024) 110376.
[51] K. Wang, H. Zhang, Gu. Xin, X.W.K. Wang, H. Zhang, Gu. Xin, X. Wang, Experimental and numerical investigations on the interface characteristics of laser impact-welded Ti/brass joints, J. Mater. Eng. Perform. 30 (2021) 1245–1258.
[52] L. Zhou, Z.Y. Li, X.G. Song, C.W. Tan, Z.Z. He, Y.X. Huang, J.C. Feng, Influence of laser offset on laser welding-brazing of Al/brass dissimilar alloys, J. Alloy. Compd. 717 (15) (2017) 78–92.